Chemical Engineering Journal 479 (2024) 147704

Contents lists available at ScienceDirect

Chemical Engineering Journal

journal homepage: www.elsevier.com/locate/cej

NIR-II excitation self-assembly nanomedicine for targeted NIR-IIa fluorescence imaging-guided cuproptosis-promoted synergistic therapy against triple-negative breast cancer

Yeneng Dai [a,b], Dongliang Leng [a,b], Ziang Guo [a,b], Jiaqi Wang [a,b], Yuheng Gu [a,b], Yingjun Peng [a,b], Lipeng Zhu [c,*], Qi Zhao [a,b,*]

[a] *Cancer Centre, Institute of Translational Medicine, Faculty of Health Sciences, University of Macau, Macau SAR 999078, China*
[b] *MoE Frontiers Science Center for Precision Oncology, University of Macau, Taipa, Macau SAR 999078, China*
[c] *School of Life Sciences, Central South University, Changsha 410013, China*

ARTICLE INFO

Keywords:
NIR-II excitation
Self-assembly
Amplified cuproptosis
NIR-IIa fluorescence imaging
Targeted therapy

ABSTRACT

Owing to easy copper efflux, the deficiency of targeting delivery and limited tissue penetration depth of light, the combination therapy of cuproptosis and phototheranostics remains enormous challenges towards triple-negative breast cancer (TNBC). To overcome these obstacles, a NIR-II excitation multifunctional nanomedicine is prepared by self-assembly of targeting aptamers (AS1411) utilizes metallic copper ions as coordination nodes, followed by coated with ultrasmall NIR-II polymer dots (Pdots) with excellent optical performances, forming a carrier-free hybrid nanosystem. After positive targeting into TNBC through specific recognition of aptamer towards cell surface nucleolin, Pdots loaded in nanomedicine enable NIR-IIa fluorescence/NIR-II photoacoustic imaging-guided NIR-II photothermal therapy (PTT) under NIR-II (1064 nm) light excitation, achieving precise phototheranostics of TNBC tumors. The loaded Cu(II) is reduced to cytotoxic Cu(I) by intracellular glutathione (GSH) and ferredoxin 1 (FDX1), synchronously enabling chemodynamic therapy (CDT) and inducing cuproptosis against TNBC. NIR-II PTT and GSH depletion further enhance therapeutic efficiency of CDT and cuprptosis through cell sensitization. This work provides a new attempt to integrate NIR-II phototheranostics and cuproptosis into a single nanoplatform with targeting capability for synergistic therapy of TNBC.

1. Introduction

As the most malignant subtype of breast cancer, triple-negative breast cancer (TNBC) tumors tend to spread to other healthy organs and relapse after treatments [1,2]. Chemotherapy is currently still main treatment modality of TNBC in clinical. Unfortunately, it is failed to improve life quality of breast cancer patients by systemic administration due to severe side effects, the occurrence of acquired drug resistance and non-specific drug biodistribution [3,4]. Therefore, the development of a non-invasive and spatiotemporally controlled treatment strategy with tumor targeting is of great importance for TNBC treatment.

Phototheranostics have experienced a vigorous development in the past few years, which can provide precise photothermal therapy (PTT) guided by real-time diagnosis through fluorescence imaging (FI) and photoacoustic imaging (PAI) under photon excitation [5–7]. Near-infrared (NIR) light excited phototheranostics towards TNBC have garnered considerable attention due to their inherent advantages of non-invasiveness and spatiotemporal controllability [8–10]. In particular, NIR-II (1000–1700 nm) light excitation phototheranostics have presented irreplaceable merits over NIR-I (700–900 nm) light, considering their deeper tissue penetration, permitting maximum permissible exposure (MPE) density, higher imaging resolution and signal-to-background ratio (SBR) [11,12], especially FI with lower tissue autofluorescence in the NIR-IIa (1300–1400 nm) subwindow [13–15]. Among various NIR-II phototheranostic agents, organic semiconducting polymers (SPs) become promising candidates owing to their good biocompatibility, high absorption coefficient as well as tunable optical properties [16–18]. Recently, NIR-II excitation PAI/PTT has been easily realized. However, it remains challenging to achieve NIR-II excitation FI on semiconducting polymers owing to the competitive photophysical

---

* Corresponding authors at: Cancer Centre, Institute of Translational Medicine, Faculty of Health Sciences, University of Macau, Macau SAR 999078, China (Qi Zhao).

E-mail addresses: zhuleaper@csu.edu.cn (L. Zhu), qizhao@um.edu.mo (Q. Zhao).

https://doi.org/10.1016/j.cej.2023.147704
Received 20 September 2023; Received in revised form 4 November 2023; Accepted 26 November 2023

process between radiative transitions and nonradiative transitions [19,20]. Furthermore, the therapeutic effect of a single phototherapy modality is unsatisfactory due to the heterogeneity and recurrence of tumor tissues.

Cuproptosis, as a unique cell death pathway, is distinguishing from known pathways such as necroptosis, ferroptosis and apoptosis [21]. It has been validated to be a promising strategy for tumor treatment and expected as a powerful assistance of phototheranostics [22,23]. Cuproptosis is a copper induced cell death pathway occurring in the tricarboxylic acid (TCA) cycle, involving in mitochondrial lipoylated protein aggregation accompanied by the loss of iron-sulfur (Fe-S) cluster proteins. The binding of lipoylated components and copper will cause high proteotoxic stress and eventual cell death [24–26]. Furthermore, it has been widely reported that copper ions can severe an oxidative stress inducer for chemodynamic therapy (CDT) through Fenton-like reaction induced hydroxyl radicals (·OH) generation in tumor tissues, which can effectively induce cellular oxidative stress and enhance the therapeutic effect of cuproptosis [27,28]. However, copper-mediated cell death is significantly restricted by intracellular glutathione (GSH) due to the copper-chelation and ·OH scavenging abilities of GSH [29,30]. Moreover, the easy transport out of tumor cells and the lack of targeted copper delivery may attenuate Cu-based therapeutic efficacy and cause copper toxicity to healthy tissues [31,32]. Therefore, the selective delivery of copper to targeted sites and intracellular GSH depletion are expected to promote copper-based cell death as well as avoiding potential toxicity. Recently, molecular engineering of nucleic acid self-assemblies has been proposed for gene interference therapy and targeted therapy in clinical practice due to high affinity and specificity [33–35], which are expected to become potential candidate of targeted delivery of copper ions for tumor-specific theranostics.

Herein, inspired by NIR-II excitation semiconducting polymers with NIR-IIa fluorescence imaging ability, a NIR-II excitation self-assembly

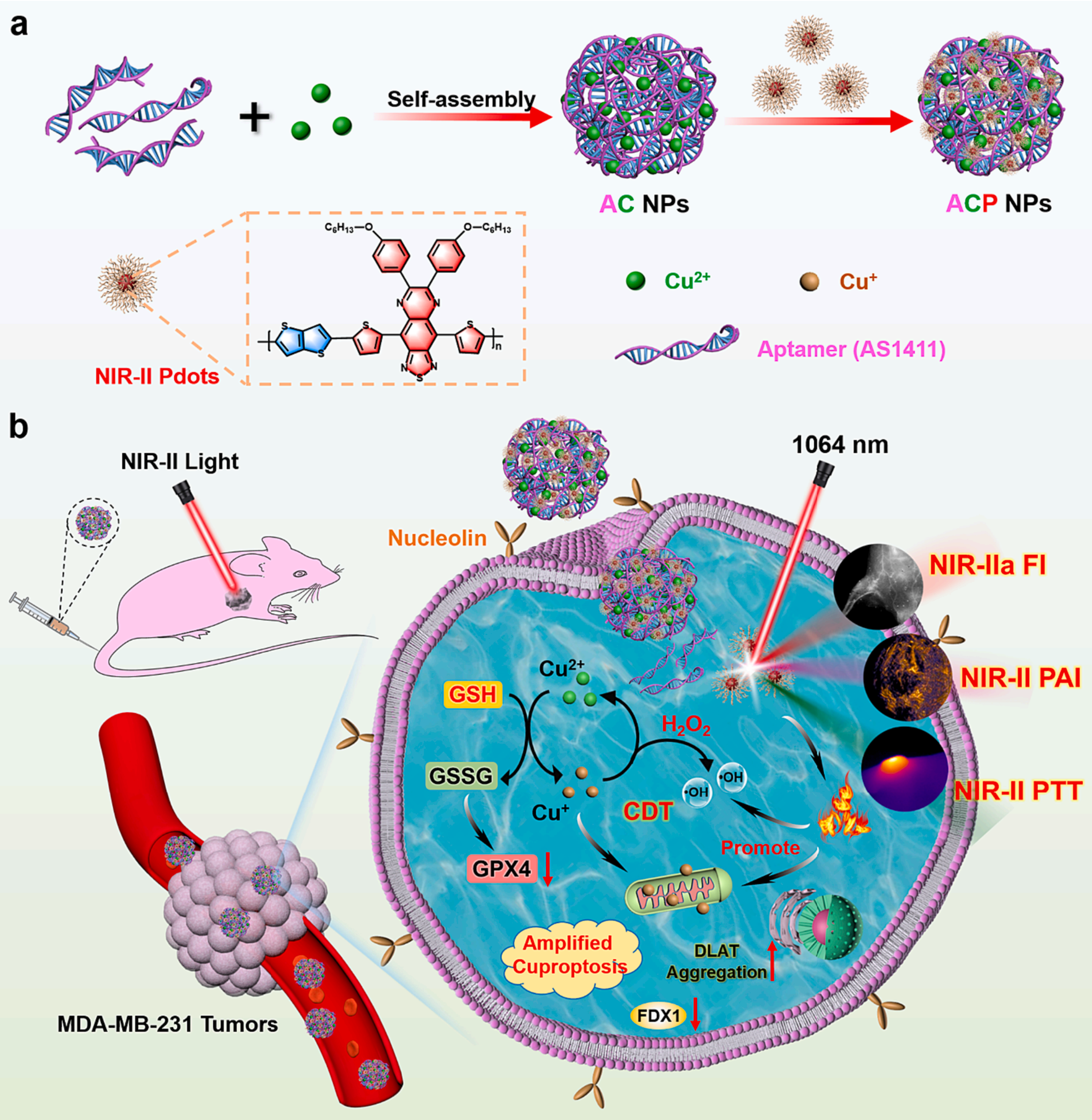

Scheme 1. Schematic illustration of self-assembly nanomedicine for synergistic therapy of TNBC. (a) Synthesis and chemical structure of ACP NPs. (b) NIR-II excitation NIR-IIa FI/NIR-II PAI-guided synergistic NIR-II PTT, chemodynamic therapy and cuproptosis against TNBC tumors.

nanomedicine (ACP NPs) with tumor-targeting ability was successfully fabricated through the copper-mediated coordinative self-assembly of aptamers (AS1411) and subsequent coating of ultrasmall NIR-II polymer dots (NIR-II Pdots), for targeted self-delivery of copper ions and NIR-II light (1064 nm) excitation photodiagnostics and promoted cuproptosis therapy against TNBC (Scheme 1). AS1411 self-assembly can mediate active targeting to TNBC cells with overexpressed nucleolin, which can specifically recognize and bind aptamers. Pdots loaded in hybrid NPs enable precise phototheranostics of TNBC through NIR-IIa FI/NIR-II PAI-guided NIR-II PTT. Furthermore, overexpressed GSH and high level of ferredoxin 1 (FDX1) reduce Cu(II) to cytotoxic Cu(I) in tumor cells. Cu (I) can not only catalyze endogenous hydrogen peroxide (H_2O_2) to generate ·OH for efficient CDT, but also bind to lipoylated components within mitochondria, leading to abnormal aggregation of dihydrolipoamide S-acetyltransferase (DLAT) and thus inducing cuproptosis through proteotoxic stress. The NIR-II photothermal effect and GSH depletion can amplify the therapeutic effect of copper-mediated oxidative stress and cuproptosis, augmenting therapeutic efficiency of TNBC. This work proposes a new integration of phototheranostics and cuproptosis into a single NIR-II light excitation nanoplatform with tumor targeting capabilities.

2. Results and discussion

2.1. Synthesis and characterization of NIR-II semiconducting polymer

Palladium-catalyzed Stille coupling polymerization was used for the synthesis of the novel semiconducting polymer (PDT-TTQ) through the conjugation between strong electron-donating unit 2,5-bis(trimethylstannyl) thieno [3,2-b]thiophene (DT) and strong electron-withdrawing unit 6,7-Bis(4-(hexyloxy)phenyl)-4,9-di(thiophen-2-yl)-[1,2,5]thiadiazolo [3,4-g]quinoxaline (TTQ) (Scheme S1). PDT-TTQ possessed the D-A-D alternating chemical backbone, which was soluble in tetrahydrofuran (THF), presenting a transparent brown color (Fig. 1a). The resulting chemical backbone was characterized by ^{1}H NMR spectroscopy (Fig. S1). The prominent peak from 0.8 to 2.0 ppm demonstrated the hydrogen signals of the alkyl chains within the thiadiazoloquinoxaline segment. 6.5 to 7.0 ppm represented the hydrogen signals from thiophene groups. Gel permeation chromatography (GPC) measurements exhibited large molecular weight with a polydispersity index (PDI) of 1.551 (Fig. S2). These results confirmed the successful synthesis of PDT-TTQ.

The optical properties of PDT-TTQ were further characterized, exhibiting the broadband optical absorption in the NIR-II window and a strong absorption at 1064 nm (Fig. 1b). The mass extinction coefficient of the polymer in THF was estimated to be 8.63 L/g cm^{-1} at 1064 nm (Fig. S3). Density functional theory (DFT) calculations were used to investigate the relationship between the chemical structure and optical properties of polymers. As shown optimized ground state (S_0) in Fig. 1c, the planar dual-thiophene unit from electron donor DT endowed the polymer with more planar structure, displaying small dihedral torsion angles less than 20° throughout the main chain. This would extend the absorption range of the conjugated backbone due to increased π-conjugation resulted from the molecular planarity, which was confirmed by decreased bandgap between highest occupied molecular orbitals (HOMOs) and the lowest unoccupied molecular orbitals (LUMOs). The presence of terminal nonconjugated alkyl chains in TTQ can enhance the intramolecular steric hindrance of the polymer through a more twisted configuration, which will facilitate improved radiative decay to generate fluorescence performance [15]. Based on such analysis, NIR-I (808 nm) light excitation fluorescence spectrum of PDT-TTQ showed a prominent fluorescence emission in the NIR-II region (Fig. 1d), with fluorescence emission peaks at approximately 1020 nm and 1310 nm. Importantly, NIR-II light (1064 nm) excitation fluorescence displayed a wide fluorescence emission range at 1200 ~ 1400 nm, especially in the NIR-IIa subwindow (Fig. 1e). NIR-IIa FI of PDT-TTQ exhibited a concentration-dependent fluorescence enhancement under 1064 nm excitation (Fig. S4). These results imply the great potential of PDT-TTQ as a NIR-II phototheranostic reagent for precise diagnosis of deep-seated tumors excited by single NIR-II light, with deeper tissue penetration depth and lower tissue autofluorescence.

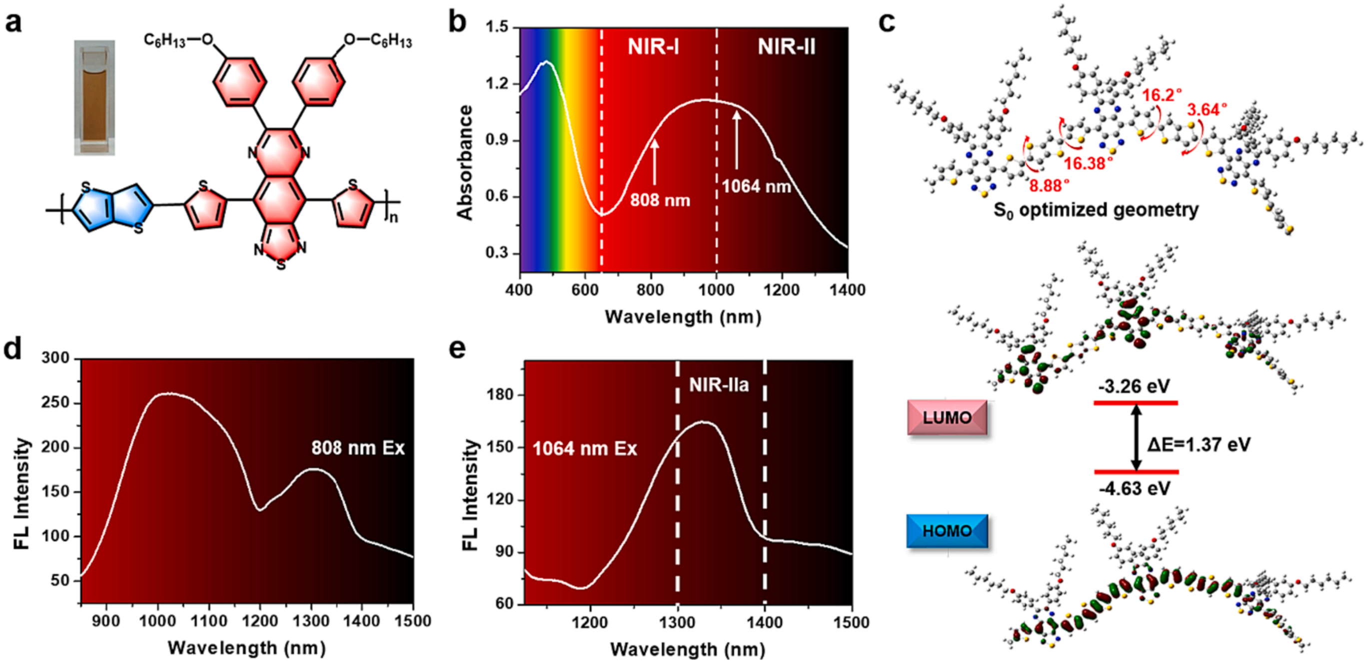

Fig. 1. The characterization of semiconducting polymer PDT-TTQ. (a) The chemical structure and solution color, (b) the absorption spectrum of PDT-TTQ dissolved in THF. (c) Optimized S_0 geometries and the HOMO-LUMO distribution from theoretical calculation at the B3LYP/6-311G(d) level in THF. (d) (e) Fluorescence emission spectra of PDT-TTQ under 808 nm and 1064 nm excitation, respectively.

2.2. Preparation and characterization of NIR-II excitation self-assembly nanomedicine

Ultrasmall NIR-II Pdots were prepared by a facile nanoprecipitation method (Fig. S5a), and large aggregates were avoided by introducing Triton X-100 during polymer encapsulation and solvent removal [36]. Pdots showed the uniform and spherical morphology with an ultrasmall size through transmission electron microscopy (TEM) images (Fig. S5b). An average size of approximately 8 nm was obtained by dynamic light scattering (DLS), with a PDI value of 0.295 (Fig. S5c). According to the investigation of photophysical properties, Pdots possess a prominent absorption at 1064 nm due to the low bandgap of the polymer (Fig. S6a). In addition, 1064 nm excitation fluorescence emission spectrum showed a broad fluorescence emission in the NIR-IIa region, implying the potential of Pdots for NIR-IIa FI of deep-seated tumors (Fig. S6b).

NIR-II excitation aptamer self-assmbly nanomedicine with tumor targeting ability was prepared by copper-mediated self-assembly of aptamer AS1411 and subsequent modification of ultrasmall Pdots utilizing coordination interactions, enabling carrier-free intracellular targeted self-delivery of payloads (Fig. 2a). Self-assembly of aptamers into monodisperse spherical nanoparticles (AC NPs) were first prepared through the charge interaction of negative aptamers and positive Cu(II) ions. AC NPs showed a uniform and monodispersed spherical morphology by TEM image, with a diameter of about 91.28 nm (Fig. S7). In addition, NIR-II Pdots can self-assemble into nanoparticles using Cu (II) as coordination nodes according to our previous work [37], and its morphology and size were similar to those of AC NPs (Fig. S8). After further surface modification of Pdots, the aptamer nanomedicine endowed with NIR-II phototheranostic performance was successfully prepared. Pdots uniformly dispersed on the surface of AC NPs through

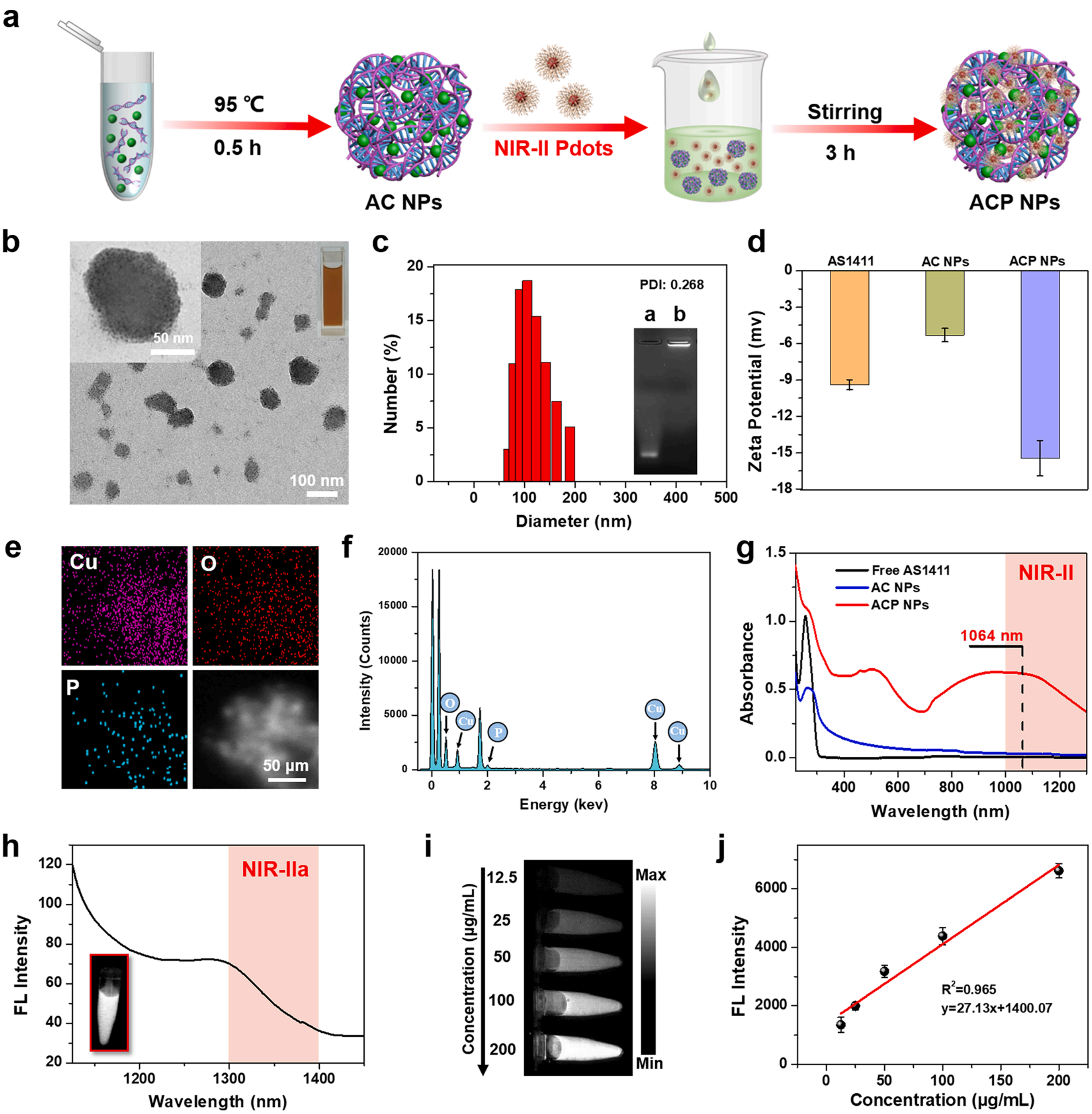

Fig. 2. Preparation and Characterization of aptamer self-assembly nanomedicine. (a) The scheme of the preparation procedure of self-assembly ACP NPs. (b) TEM images, (c) size distribution and agarose gel electrophoresis (inset, a: free AS1411, b: ACP NPs) of ACP NPs. (d) Zeta potential of different components. (e) TEM-EDS elemental mapping images and (f) EDX spectrum of ACP NPs. (g) UV–vis absorption spectra of aptamer-relative nanomedicines. (h) 1064 nm laser excited fluorescence emission spectrum of ACP NPs. (i) Concentration dependent NIR-II FI and (j) fluorescence intensity analysis of ACP NPs aqueous solution excited by 1064 nm laser.

the interaction of Cu(II) and Pdots, and ACP NPs aqueous solution exhibiting a brown color (Fig. 2b). The diameter of ACP NPs increased to about 105.7 nm compared with AC NPs (Fig. 2c), and remained relatively stable within 7 days (Fig S9). According to agarose gel electrophoresis, the aptamer self-assembly nanomedicine showed slower electrophoretic mobility shift compared with the linear aptamer, possibly ascribed to the large molecular mass of ACP NPs (Fig. 2c). Due to the coordination of Cu(II) and the phosphate groups of the aptamer, the potential of AC NPs showed a slight increase from −9.4 mV to −5.3 mV. However, the potential of ACP NPs was further reduced to −15.45 mV due to the introduction of Pdots with large amounts of negative charges (Fig. 2d). The element mapping and energy-dispersive X-ray spectroscopy (EDX) showed that the elemental Cu, O and P were symmetrically distributed in ACP NPs (Fig. 2e and Fig. 2f), confirming the successful preparation of copper-based nanomedicine. The copper content of ACP NPs was determined to be 55.6 wt%, and the loading efficiency of aptamer AS1411 was calculated to be approximately 62.72 %. In order to achieve NIR-II phototheranostics, the photophysical properties of aptamer nanomedicines were further explored. As shown in Fig. 2g, AC NPs showed the characteristic absorption peak of aptamer AS1411 at 260 nm. The successful modification of Pdots endowed ACP NPs with broad absorption extending to 1300 nm, with a strong absorption and a mass extinction coefficient of 8.94 L/g cm^{-1} at 1064 nm (Fig. S10). Moreover, under 1064 nm excitation, ACP NPs emitted obvious NIR-II fluorescence even extending to 1400 nm (Fig. 2h). The 1064 nm excited NIR-IIa FI revealed the polymer concentration-dependent NIR-IIa fluorescence enhancement of ACP NPs solution, evidenced by gradual enhanced fluorescence intensity (Fig. 2i and Fig. 2j). These results suggested that the integration of targeting aptamers and NIR-II phototheranostic agents enables ACP NPs an excellent candidate for single NIR-II light excitation tumor-targeted multimodal theranostics.

2.3. *NIR-II photothermal effect and photothermal promoted ·OH production*

In order to investigate NIR-II excitation photothermal efficiency of ACP NPs, 1064 nm laser irradiation was performed on ACP NPs aqueous solution for 5 min (1.0 W/cm^2). Obviously, time- and concentration-dependent rapid heat variation was observed. ACP NPs reached the maximum temperature of 66.7 ℃ when the polymer concentration was 100 μg/mL (Fig. 3a). Significant changes in infrared thermal images over concentrations and irradiation time demonstrated the excellent photothermal conversion capability of ACP NPs (Fig. 3b). The photothermal stability of ACP NPs was evaluated by the monitoring the recycling temperature changes of ACP NPs aqueous solution under consecutive 1064 nm laser on/off irradiation. During four consecutive light on/off cycles, the temperature of ACP NPs did not display any distinct attenuation (Fig. 3c), indicating the high photothermal stability of ACP NPs. A heating/cooling cycle revealed that the photothermal

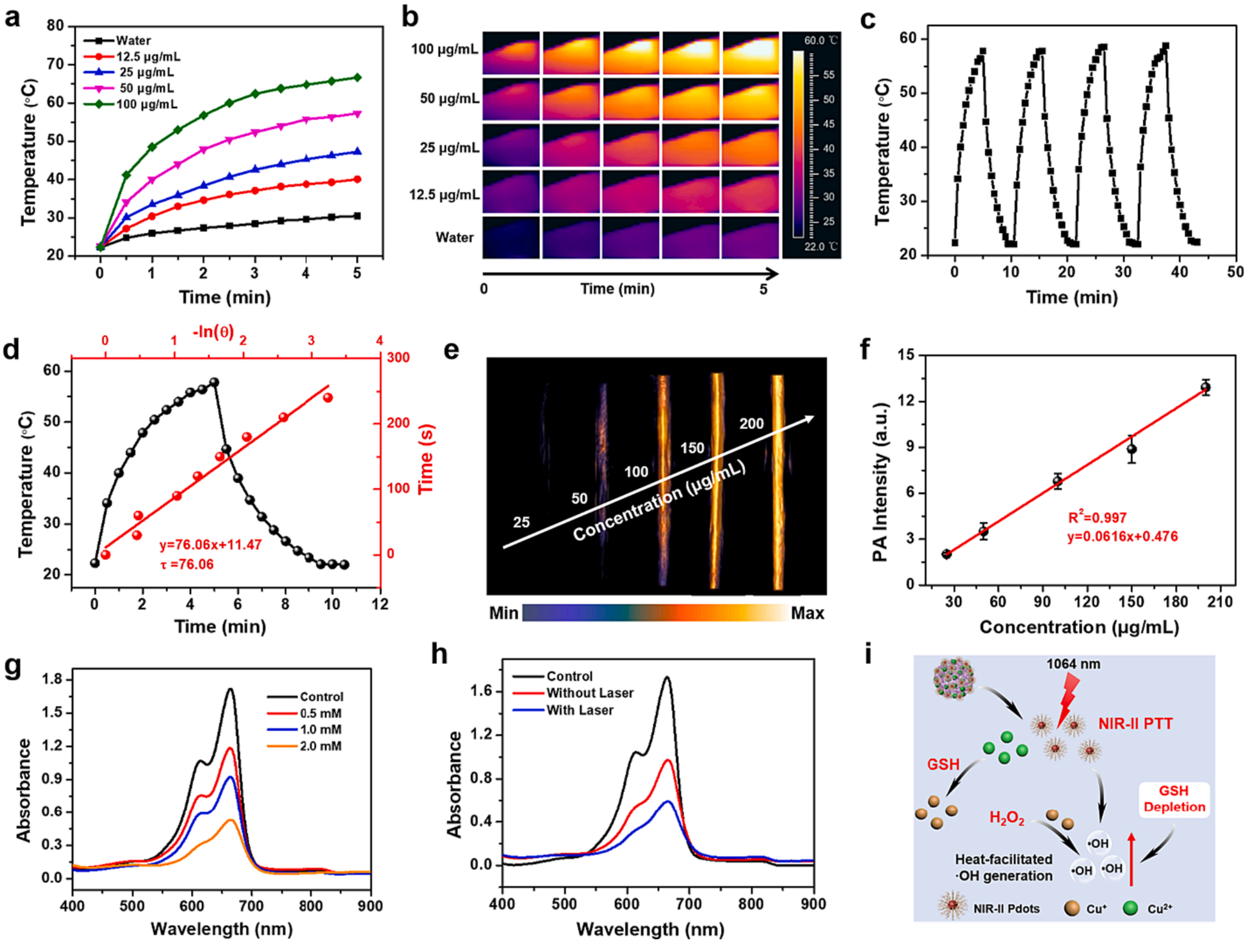

Fig. 3. NIR-II photothermal effect and ·OH production. 1064 nm laser irradiation (1.0 W/cm^2) induced (a) temperature curves and (b) infrared thermal images of ACP NPs aqueous solution. (c) Photostability of ACP NPs solutions during four consecutive heating–cooling periods. (d) The heating–cooling curve and photothermal conversion efficiency calculations. (e) Concentration-dependent PAI and (f) photoacoustic intensity analysis of ACP NPs solutions excited by 1064 nm laser. (g) The absorption spectra of MB treated with ACP NPs and H_2O_2 (10 mM) with different concentrations of GSH. (h) 1064 nm laser irradiation (1.0 W/cm^2) induced absorption changes of the mixture solution. (i) Schematic illustration of NIR-II light triggered enhanced ·OH production.

conversion efficiency (η) of ACP NPs under 1064 nm excitation was approximately 37.76 % (Fig. 3d). These results lay a solid foundation for NIR-II excitation photothermal therapy for tumor ablation *in vivo* through high photothermal conversion outputs of ACP NPs. Inspired by the prominent light-harvesting capability at 1064 nm, *in vitro* photoacoustic imaging of ACP NPs was further evaluated. Under 1064 nm laser excitation, ACP NPs solution presented concentration-related gradually enhanced PA images (Fig. 3e). This was evidenced by a linear relationship between PA intensity and concentration (Fig. 3f), suggesting great application promise of ACP NPs as a NIR-II PA agent.

Next, the ability of ACP NPs catalyzing H_2O_2 to generate ·OH through Fenton-like reaction was evaluated. ·OH generation was detected using methylene blue (MB) as an indicator through the decrease of absorption. The mixture solutions of MB and H_2O_2 were incubated with ACP NPs in the presence of GSH (0 ~ 2 mM). The absorption of MB gradually decreased as GSH concentrations increased (Fig. 3g), which may be attributed to GSH-triggered promoted reduction of Cu(II) to Cu(I) participating in the Fenton-like reaction, thus producing more ·OH. Such GSH consumption can avoid the elimination of ·OH via the redox, thus producing more reactive oxygen species (ROS) for tumor apoptosis. The dynamic degradation process of MB induced by ·OH was monitored in the presence of 2 mM GSH, exhibiting time-dependent MB degradation and indicating the consecutive ·OH production. After 120 min incubation, the absorption of MB at 665 nm decreased approximately 3.14-fold relative to that at 0 min, which was further evidenced by color changes of the solution (Fig. S11). To investigate the influence of NIR-II irradiation on ·OH generation, the mixture solution was irradiated by 1064 nm laser for 10 min. A more significant absorption decrease indicated that NIR-II laser irradiation can remarkably enhance ·OH production (Fig. 3h), which may be ascribed to that NIR-II photothermal effect induced hyperthermia promotes the catalytic rate of Fenton-like reaction. These results confirmed that ACP NPs can serve as a nanoreactor to achieve enhanced ·OH generation for amplifying anti-tumor oxidative stress through NIR-II photothermal effects and GSH consumption (Fig. 3i).

2.4. *Cell targeted uptake and intracellular ROS generation*

Due to the specific recognition of aptamer AS1411 to nucleolin overexpressed on the surface of TNBC cells. ACP NPs mediated active targeting towards TNBC cells was evaluated. ACP NPs were doped with the fluorescent dye RhB, and the absorption and emission spectra were shown in Fig. S12. After RhB doping, ACP NPs modified by AS1411 and CP NPs without AS1411 modification were added to MDA-MB-231 cells, respectively. In addition, blocking experiments were conducted by the addition of excess AS1411 beforehand. As shown in Fig. 4a, more fluorescence of RhB was observed in the cytoplasm of ACP NPs-treated cells compared with the other groups, indicating an improved endocytosis of ACP NPs into tumor cells. Normal human embryonic kidney cells, 293 T cells were selected as another comparison group, exhibiting negligible fluorescence after incubated with ACP NPs due to the absence of nucleolin. Flow cytometry analysis further showed the proportion of MDA-MB-231 cells with ACP NPs increased 2.94-fold and 6.59-fold, respectively, compared with those with AS1411 blockade and CP NPs

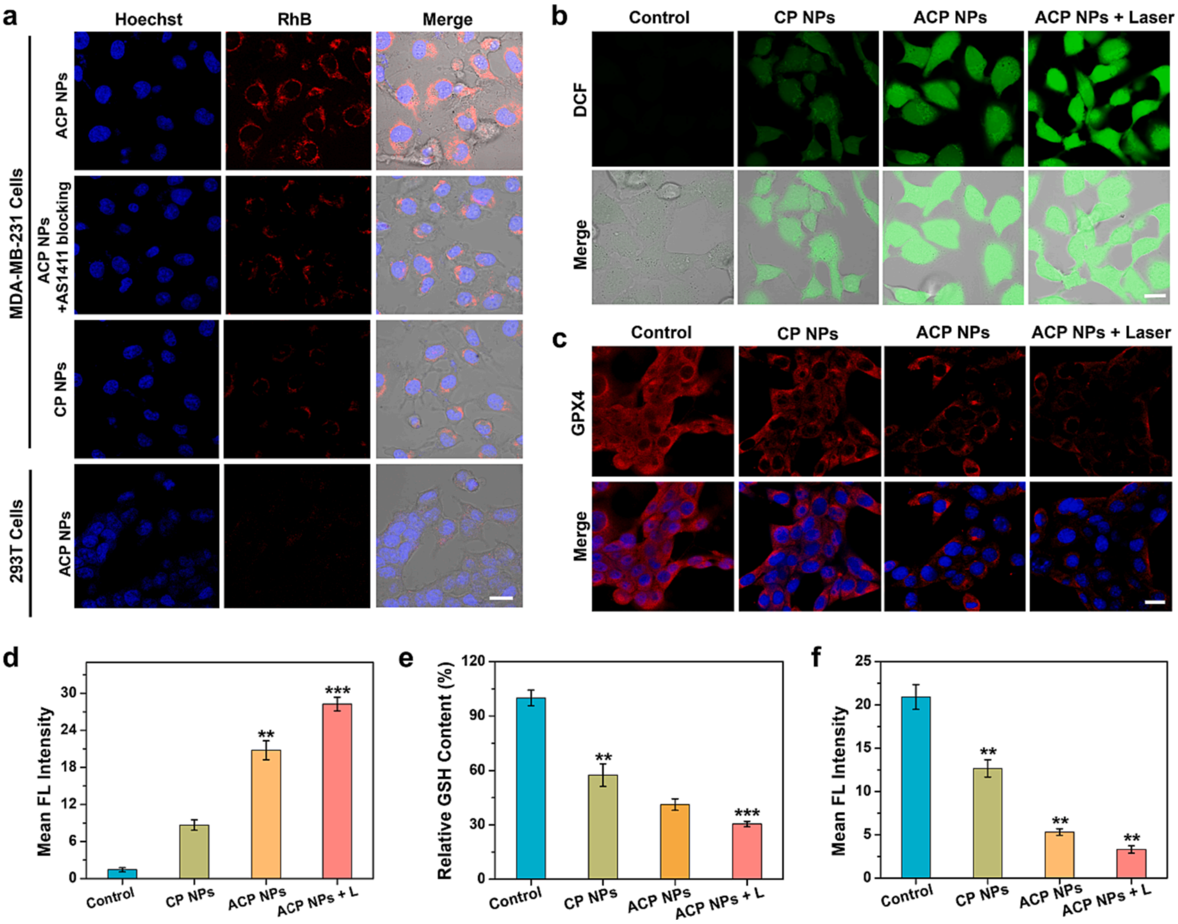

Fig. 4. Evaluation of intracellular uptake and ROS production. (a) Intracellular fluorescence of MDA-MB-231 cells and 293 T cells with different treatments. Scale bar: 20 μm. (b) Various treatments induced intracellular ROS levels and (d) mean fluorescence intensity. Scale bar: 20 μm. (c) Immunofluorescence images and (f) fluorescence intensity analysis of GPX4 levels in cells with various treatments. Scale bar: 20 μm. (e) Relative GSH content within tumor cells subjected to various treatments. ($^{**}p < 0.01$, $^{***}p < 0.001$).

(Fig. S13). The intracellular fluorescence of MDA-MB-231 cells treated with ACP NPs doped with RhB was detected at different incubation time points. As shown in Fig. S14, ACP NPs gradually migrated from endolysosomes to the periphery of the cell nucleus, as evidenced by enhanced fluorescence of RhB in cells. These results demonstrated the positively active targeting ability of ACP NPs towards MDA-MB-231 cells owing to the specific binding between aptamer and nucleolin.

ROS generation in tumor cells was detected after various treatments using 2′, 7′-dichlorodihydrofluorescein diacetate (DCFH-DA) as ROS capture probes. MDA-MB-231 cells treated with ACP NPs displayed brighter green fluorescence compared with cells treated with CP NPs (Fig. 4b), which was evidenced by quantitative fluorescence intensity (Fig. 4d), indicating more ROS production due to AS1411-mediated active targeting. Notably, 1064 nm laser irradiation endowed ACP NPs treated cells with the highest fluorescence level, with a 1.36-fold enhancement of fluorescence intensity compared with cells treated with ACP NPs, which might be ascribed to NIR-II photothermal effect promoted intracellular Fenton-like reaction. These results suggested that ACP NPs with AS1411 modification and NIR-II laser irradiation could significantly enhance the ROS levels in MDA-MB-231 cells. After targeting into tumor cells of ACP NPs, overexpressed GSH in tumor cells can reduce Cu(II) to cytotoxic Cu(I) to induce cuproptosis through the aggregation of lipoylated DLAT and intracellular oxidative stress through increased ROS levels. The content of intracellular GSH was detected by DTNB assay after various treatments. GSH levels in cells treated by ACP NPs with laser irradiation significantly decreased by 3.27-fold relative to that of the control group (Fig. 4e). GSH depletion would lead to the down-regulation of glutathione peroxidase 4 (GPX4), which can reduce phospholipid peroxides and weaken the oxidative stress induced by ROS. As shown in Fig. 4c, self-assembly nanomedicines containing Cu(II) significantly reduced intracellular GPX4 expression, evidenced by reduced immunofluorescence. Moreover, 1064 nm laser

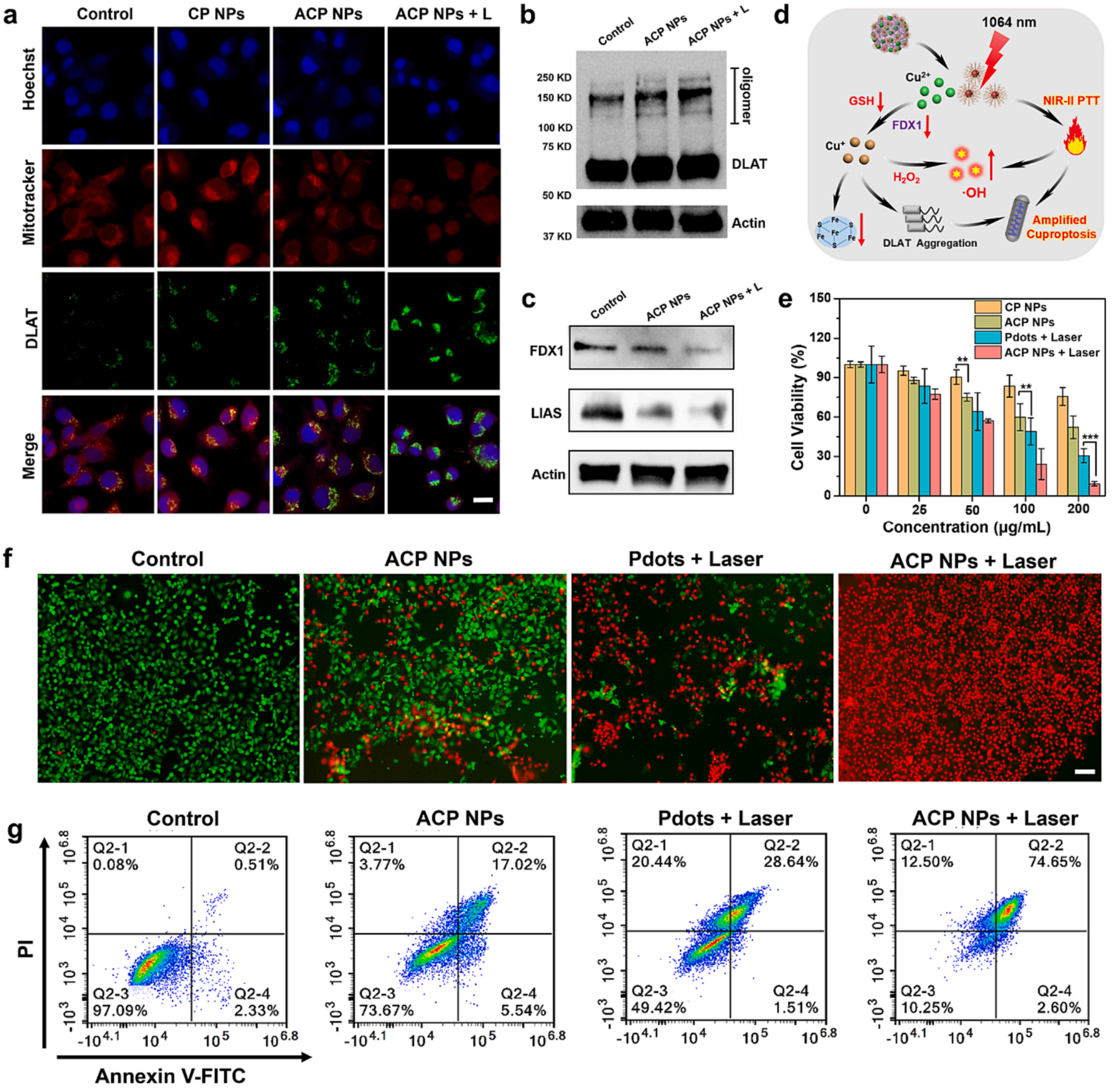

Fig. 5. Cuproptosis effect evaluation and cytotoxicity analysis of ACP NPs. (a) Immunofluorescence and (b) western blot analysis of mitochondrial DLAT. Scale bar: 20 μm. (c) Western blot analysis of Fe-S cluster protein. (d) The mechanism of NIR-II PTT and GSH depletion enhanced cuproptosis. Various treatments induced (e) cytotoxicity evaluation, (f) live/dead staining and (g) flow cytometry analysis against MDA-MB-231 cells. Scale bar: 100 μm. (**$p < 0.01$, ***$p < 0.001$).

irradiation could further enhance the down-regulation of GPX4 within tumor cells treated with ACP NPs, confirmed by the lowest fluorescence intensity (Fig. 4f).

2.5. *Validation of anti-tumor mechanism of ACP NPs-mediated cuproptosis*

In order to validate the anti-tumor mechanism of ACP NPs-mediated cuproptosis, the levels of relative mitochondrial proteins in MDA-MB-231 cells were evaluated. The aggregation of lipoylated DLAT was first detected by immunofluorescence staining. MDA-MB-231 cells treated with ACP NPs under NIR-II laser irradiation exhibited the most pronounced DLAT foci compared with other groups (Fig. 5a), ascribed to the abnormal DLAT oligomerization. Such results were further confirmed by western blot detection, the treatment with ACP NPs resulted in an obvious oligomerization of lipoylated DLAT compared with the control group. Moreover, 1064 nm laser irradiation leaded to more DLAT oligomers (Fig. 5b). Additionally, the level of Fe-S cluster protein in cells, including reductase referredoxin 1 (FDX1) and lipoyl synthase (LIAS), decreased significantly after treated with ACP NPs (Fig. 5c). In particular, most obvious disappearance of Fe-S cluster protein was found after 1064 nm laser irradiation. Therefore, ACP NPs can be used as a cuproptosis agent to induce tumor cell death through the oligomerization of DLAT protein and reduction of Fe-S cluster protein. More importantly, these phenomena also revealed NIR-II laser irradiation and GSH depletion can evoke stronger sensitiveness of tumor cells to cuproptosis, thus amplifying anti-tumor therapeutic effect (Fig. 5d).

ACP NPs-mediated cell damage was further evaluated by monitoring changes of mitochondrial membrane potential (MMP) utilizing the JC-1 probe. As shown in Fig. S15, AC NPs and ACP NPs could induce significant MMP depolarization of MDA-MB-231 cells through remarkably elevated green fluorescence of JC-1 monomers accompanied by the decrease of JC-1 aggregates, indicating severe mitochondrial damage induced by AC NPs and ACP NPs. It was worthwhile to note that mitochondrial damage become increasingly severe after treated with ACP NPs and 1064 nm laser irradiation, verified by the highest level of JC-1 monomers, which can be attributed to NIR-II irradiation induced enhanced ROS production and improved therapeutic effect of CDT.

2.6. *In vitro cytotoxicity analysis*

CCK-8 assay was adopted to evaluate the cytotoxicity mediated by ACP NPs towards MDA-MB-231 cells. As shown in Fig. 5e and Fig. S16a, CP NPs, AC NPs and ACP NPs all resulted in concentration-dependent cell death after 6 h of incubation. Furthermore, AC NPs and ACP NPs-treated cells exhibited a lower cell survival rate compared with CP NPs treatment, with a cell viability of approximately 56.55 % and 52.16 % at the high concentration, respectively, which may be attributed to AS1411-mediated more endocytosis of ACP NPs, thus producing a better therapeutic effect. Due to the lack of targeted delivery, ACP NPs showed relatively low cytotoxicity against 293 T cells compared with MDA-MB-231 cells (Fig. S16b). NIR-II laser irradiation-induced NIR-II PTT significantly enhanced the therapeutic effect of tumor cells, which was verified by lowest cell survival of approximately 9.33 % in ACP NPs-treated cells under 1064 nm laser irradiation. This may be ascribed to the synergistic therapeutic effect of NIR-II PTT, CDT and cuproptosis. Dead/live cell staining was performed to visualize cell apoptosis. The treatments of ACP NPs and Pdots plus laser irradiation caused more red fluorescence of dead cells compared with the control group (Fig. 5f), ascribed to copper-mediated cell death and NIR-II PTT, respectively. Moreover, ACP NPs plus laser irradiation resulted in the most dead cells and negligible live cells, confirming the NIR-II light excitation synergistic therapeutic effect. Additionally, flow cytometric analysis was further used for quantification of cell apoptosis (Fig. 5g). Cells treated with ACP NPs plus laser irradiation exhibited the most apoptosis, with an apoptotic ratio of approximately 89.75 % (Fig. S17), which enhanced by about 3.41 and 1.77-fold compared to cells treated with ACP NPs and Pdots plus laser irradiation, respectively. This was similar to the results of CCK-8 and staining assays. These results confirmed the great application potential of ACP NPs used for NIR-II light excitation synergistic therapy towards TNBC cells.

2.7. *NIR-IIa FI and NIR-II PAI under NIR-II excitation*

Inspired by the prominent NIR-IIa fluorescence and NIR-II photoacoustic performance *in vitro*, NIR-II light-excited FI and PAI of TNBC tumors were evaluated. ACP NPs solution (polymer: 1 mg/mL) was injected into the tail vein of mice, and the whole-body fluorescence contrast in the mouse was observed upon 1064 nm laser excitation. Owing to reduced tissue autofluorescence and photon scattering induced by long wavelengths, the whole-body vascular branches can be clearly distinguished from surrounding background tissues by NIR-IIa FI at 10 min postinjection (Fig. S18a). NIR-IIa FI of magnified abdominal and hindlimb vessels exhibited high imaging contrast (Fig. 6a and Fig. 6c), with signal-to-background ratio (SBR) of 1.57 and 12.53, respectively. The width of tagged blood vessels in the abdominal and hindlimb region was determined to be 0.851 mm and 0.628 mm, respectively, according to the full widths at half-maximum (FWHM) acquired from the fluorescence intensities along the tagged cross-sectional lines (Fig. 6b and Fig. 6d). These results implied the great promise of ACP NPs as an angiographic contrast agent through NIR-II excitation FI.

The tumor accumulation process of ACP NPs was investigated by NIR-IIa FI. As shown in Fig. 6e, after intravenous injection via the tail vein, ACP NPs began to accumulate in the liver and spleen of MDA-MB-231 tumor-bearing nude mice, and travelled through the blood circulation. At 4 h post-injection, NIR-II fluorescence at the tumor site of mice gradually brightened and reached a peak at 12 h postinjection, with an about 3.04-fold increase of fluorescence intensity compared with that at 0 h (Fig. 6f). This suggested an optimal time point for subsequent NIR-II excitation synergistic therapy due to the maximum accumulation amount of ACP NPs in the tumor region. At 24 h postinjection, more pronounced NIR-II fluorescence signals were observed in liver, spleen and tumor compared with other major organs (Fig. S18b), validated by quantitative fluorescence intensity analysis (Fig. S18c).

Next, *in vivo* NIR-II PAI ability of ACP NPs was evaluated. 1064 nm laser excitation whole-body PAI of mice was obtained after intravenous injection with ACP NPs solution. At 4–12 h postinjection, NIR-II photoacoustic signal in the tumor site gradually boosted, and the abundance of microscopic blood vessels of the tumor exhibited time-dependent enhancement, providing the distinct vascular visualization (Fig. 6g). The maximum photoacoustic signal of the tumor was obtained at 12 h post-injection, increasing by 3.83-fold that at 0 h (Fig. 6h), which was consistent with the results of NIR-IIa FI *in vivo*. These results confirmed that ACP NPs afforded the precise diagnosis of TNBC tumors before synergistic therapy, providing deeper penetration depth, higher imaging resolution and contrast.

2.8. *In vivo NIR-II excitation synergistic anti-tumor therapy*

Due to excellent therapeutic effects of NIR-II PTT enhanced CDT and cuproptosis *in vitro*, NIR-IIa FI/NIR-II PAI-guided tumor inhibition effect of ACP NPs towards TNBC was further evaluated by injection of different samples into MDA-MB-231 tumor-bearing nude mice. At 12 h post-injection (the optimal time point for drug accumulation), 1064 nm laser was performed on the tumors of mice injected with Pdots and ACP NPs for 10 min (1.0 W/cm^2), and the temperature changes in the tumor sites were continuously recorded by an infrared thermal imaging camera (Fig. 7a). Fig. 7b showed photothermal images of tumor region during laser irradiation. The temperature of both Pdots and ACP NPs-treated tumors could reach 60 °C within 3 min (Fig. 7c), enabling tumor

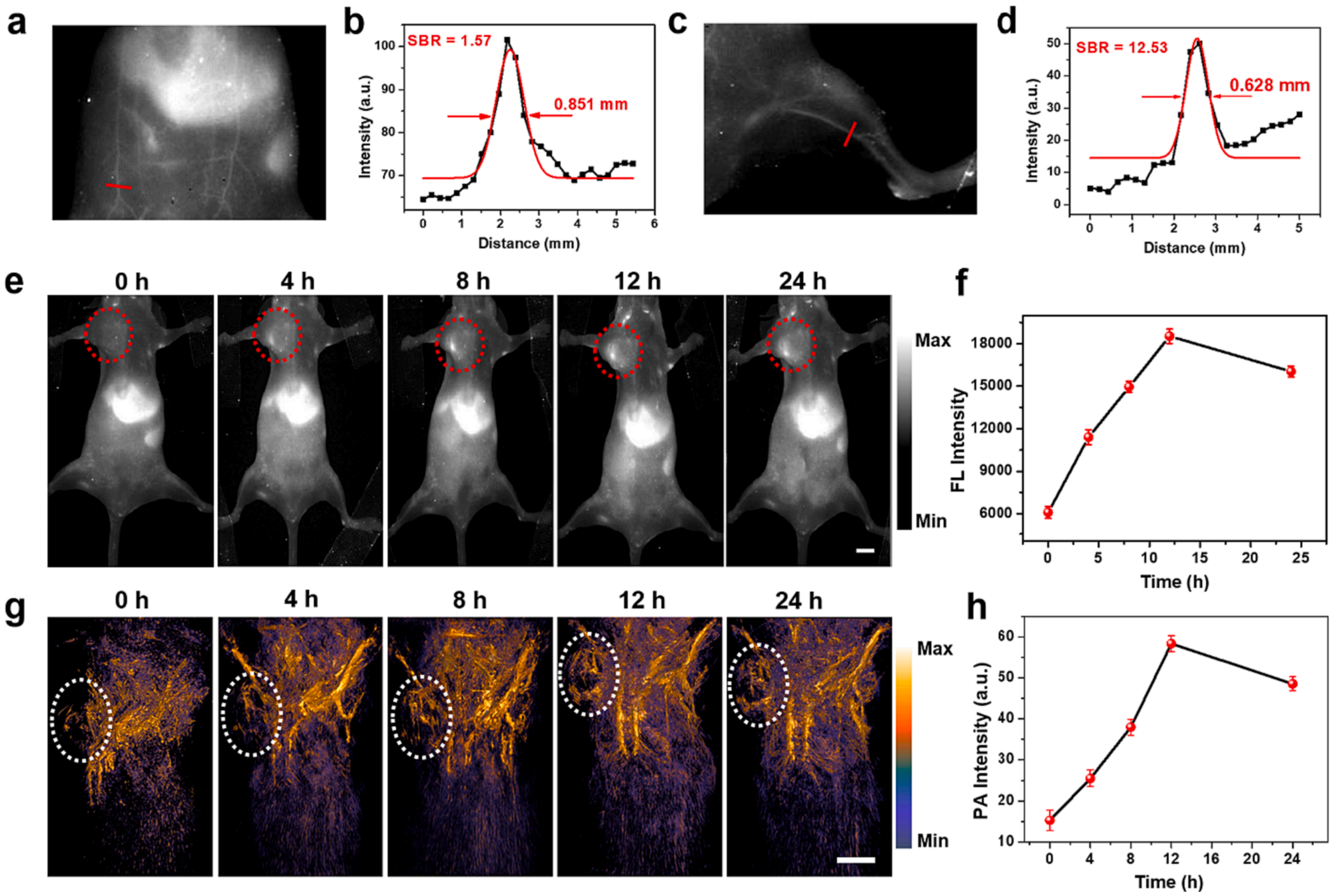

Fig. 6. *In vivo* NIR-II imaging. NIR-IIa FI of magnified (a) abdominal and (c) femoral vessels of mouse excited by 1064 nm laser, and (b) (d) corresponding intensity analysis and FWHM calculation along the marked cross-section lines by Gaussian fitting. (e) NIR-IIa FI and (g) NIR-II PAI of mice bearing with MDA-MB-231 tumors, corresponding (f) fluorescence intensity and (h) photoacoustic intensity curves of tumors over time after intravenous injection with ACP NPs. Scale bar: 5 mm.

ablation through NIR-II photothermal effects. After various treatments, the therapeutic effects were evaluated by continuously monitoring the physical parameters of the mice within 14 days. As shown in Fig. 7d, the mice treated with ACP NPs exhibited an obviously slow tumor growth, ascribed to combination therapeutic effect induced by copper-mediated CDT and cuproptosis. The tumor growth of mice treated with Pdots plus laser irradiation were effectively inhibited through NIR-II PTT. In particular, ACP NPs and laser irradiation treated tumors were almost completely inhibited compared with other groups, evidenced by the tumor volume curve almost tending to zero, which was ascribed to NIR-II light excitation synergistic therapeutic effects of NIR-II PTT, CDT and cuproptosis. After 14 days, photographs of mice and tumors showed significant differences in the tumor size among different treatment groups (Fig. 7e and Fig. 7g), which was further verified by differential tumor weights. ACP NPs plus laser irradiation enabled the tumor weight of about 0.06 g (Fig. 7f), resulting in a tumor inhibition rate of about 92.59 %. In addition, H&E and TUNEL staining of tumor tissues confirmed NIR-II PTT enhanced copper-induced cell damage through increased dead cells without nuclei (Fig. 7h). It was noted that the body weight of mice from all groups remained almost no changes over time (Fig. S19). Major organs in all groups exhibited negligible tissue damage after 14 days of treatment through H&E staining (Fig. S20), proving biocompatibility and biosafety of all samples. These results confirmed that ACP NPs can serve as a promising phototheranostic agent for *in vivo* targeted NIR-II light excitation multimodal theranostics towards TNBC tumors.

2.9. The potential therapeutic mechanism of NIR-II excitation synergistic therapy

After 14 days of treatment, mRNA sequencing of tumors treated with PBS and ACP NPs + 1064 nm Laser (the final treatment group) was performed to investigate potential therapeutic mechanisms of NIR-II excitation synergistic therapy. All sequencing data were normalized using the VST (variance stabilizing transformations) method in DESeq2 before further analyzed (Fig. S21). Based on the filtering criteria (FC $\geq$ 2.0, P $<$ 0.05), approximately 1467 significantly differentially expressed genes (DEGs) were identified between the PBS group and the ACP NPs + Laser group, including 29 up-regulated DEGs and 1438 down-regulated DEGs (Fig. 8a). Gene Ontology (GO) enrichment analysis exhibited that ACP NPs + Laser treatment significantly altered genes related to membrane potential regulation and calcium ion transport in biological processes (Fig. 8b). This may be ascribed to that ACP NPs induced enhanced ROS generation and amplified cuproptosis triggered the depolarization of mitochondrial membrane potential and overloading of calcium ion concentration, thus leading to tumor cell death. Kyoto Encyclopedia of Genes and Genomes (KEGG) pathway enrichment analysis further verified NIR-II light-excited cell apoptosis through changes of intracellular apoptosis-related signaling pathways, such as cAMP signaling pathway and calcium signaling pathway (Fig. 8c). Protein-protein interaction (PPI) network analysis based on differential genes revealed some key proteins related to calcium ion transport pathways and membrane depolarization, such as CACNA1D, CACNA1C and SCN3B (Fig. 8d). These proteins play important roles in tumor suppression. The above results illustrated that the underlying mechanism of ACP NPs + Laser induced synergistic therapy, may be related to the regulation of

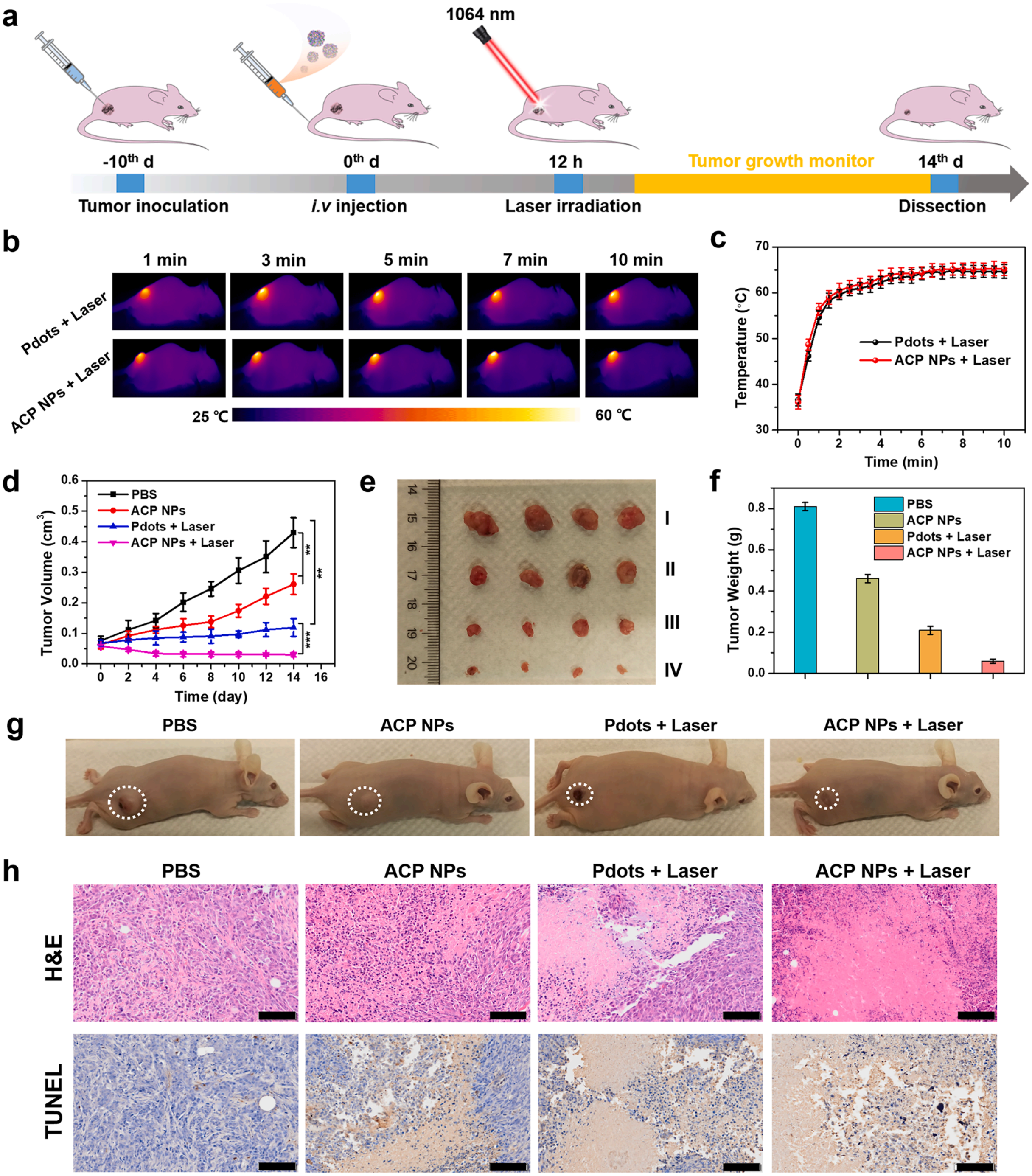

Fig. 7. NIR-II light excitation synergistic anti-tumor therapy. (a) Schematic representation of the schedule of synergistic treatment towards TNBC. (b) 1064 nm-excited thermal images and (c) temperature profiles of tumors treated with Pdots and ACP NPs. (d) Tumor volume curves over time after various treatments. (e) Tumor photograph, (f) tumor weight and (g) representative mouse photographs in each group after various treatments. (h) H&E and TUNEL staining images of tumors in all of groups. (I) PBS; (II) ACP NPs; (III) Pdots + Laser; (IV) ACP NPs + Laser. Scale bar: 100 μm.

intracellular membrane potential and calcium ion signaling pathways.

3. Conclusion

In summary, a NIR-II excitation phototheranostic nanoplatform (ACP NPs) was successfully developed through metal copper-mediated coordination self-assembly of aptamers, followed by modification of ultrasmall NIR-II Pdots, forming an NIR-II self-assembly nanomedicine as a carrier-free nanosystem for targeting self-delivery of payloads and NIR-II excitation multimodal phototheranostics towards TNBC. ACP NPs can improve tumor accumulation through aptamer-mediated active targeting, enabling NIR-IIa FI/NIR-II PAI-guided NIR-II PTT and copper-mediated chemodynamic and cuproptosis therapy. The levels of intracellular oxidative stress and cuproptosis were further amplified by the NIR-II photothermal effect and GSH depletion, provoking a synergistic therapeutic effect of TNBC. This work proposed a new integration strategy between NIR-II excitation phototheranostics and cuproptosis, simultaneously with positive tumor targeting capabilities.

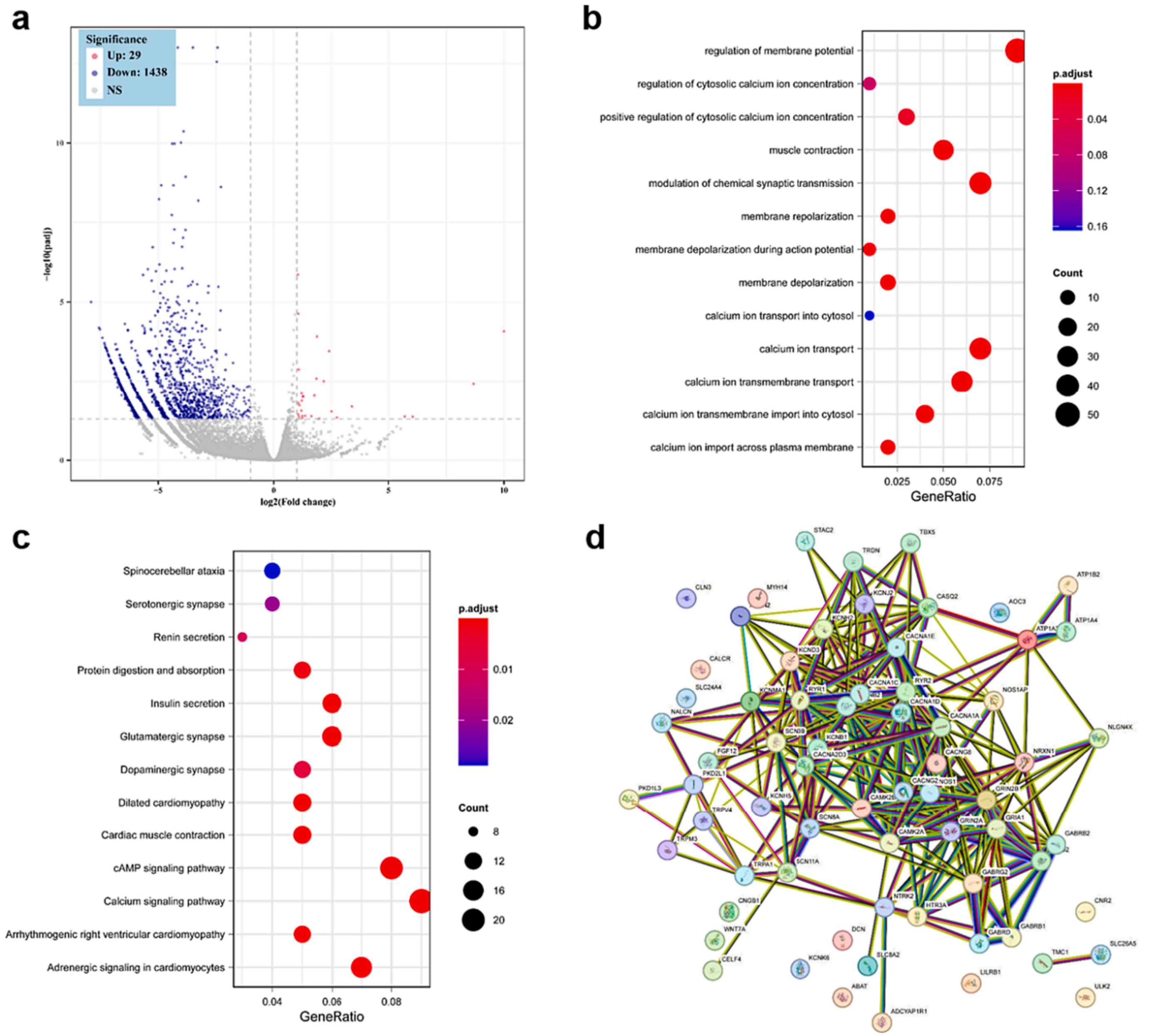

Fig. 8. mRNA sequencing analysis in control PBS and ACP NPs + Laser group. (a) Volcano map of DEGs between PBS group and ACP NPs + Laser group. (b) GO enrichment analysis and (c) KEGG pathway enrichment analysis through DEGs between the control and ACP NPs + Laser group. (d) PPI analysis based on the DEGs in the biological process.

Declaration of competing interest

The authors declare that they have no known competing financial interests or personal relationships that could have appeared to influence the work reported in this paper.

Data availability

Data will be made available on request.

Acknowledgments

This work was financially supported by the National Key R&D Program of China (2019YFA0904400), the Natural Science Foundation of Guangdong Province (2023A1515010549), the Science and Technology Development Fund of Macau (FDCT/0043/2021/A1 and FDCT/0002/2021/AKP), the University of Macau (MYRG2022-00143-FHS), Dr. Stanley Ho Medical Development Foundation (SHMDF-VSEP/2022/002), Zhong Nanshan Medical Foundation of Guangdong Province (ZNSA-2021016).

Appendix A. Supplementary data

Supplementary data to this article can be found online at https://doi.org/10.1016/j.cej.2023.147704.

References

[1] J.X. He, T.H. Peng, Y.B. Peng, L.L. Ai, Z.Y. Deng, X.Q. Wang, W.H. Tan, Molecularly engineering triptolide with aptamers for high specificity and cytotoxicity for triple-negative breast cancer, J. Am. Chem. Soc. 142 (2020) 2699–2703.

[2] L.J. Zeng, S.S. Ding, Y.H. Cao, C.L. Li, B. Zhao, Z.L. Ma, J.R. Zhou, Y.P. Hu, X. Zhang, Y. Yang, G.J. Duan, X.W. Bian, G. Tian, A MOF-based potent ferroptosis

inducer for enhanced radiotherapy of triple negative breast cancer, ACS Nano 17 (2023) 13195–13210.

[3] M.Z. Lin, Y.J. Cai, G.J. Chen, H.H. Zhong, B. Li, T. Li, Z.C. Xiao, X.T. Shuai, A hierarchical tumor-targeting strategy for eliciting potent antitumor immunity against triple negative breast cancer, Biomater. 296 (2023), 122067.

[4] A. Lee, M.B.A. Djamgoz, Triple negative breast cancer: Emerging therapeutic modalities and novel combination therapies, Cancer Treat. Rev. 62 (2018) 110–122.

[5] Y.E. Dai, X.Y. Li, Y.W. Xue, K. Chen, G.D. Jiao, L.P. Zhu, M.X. Li, Q.L. Fan, Y.L. Dai, Q. Zhao, Q.M. Shen, Self-delivery of metal-coordinated NIR-II nanoadjuvants for multimodal imaging-guided photothermal-chemodynamic amplified immunotherapy, Acta Biomater. 166 (2023) 496–511.

[6] T.W. Li, K.L. Cao, X.H. Yang, Y.Y. Liu, X.Y. Wang, F. Wu, G.C. Chen, Q.B. Wang, An oral ratiometric NIR-II fluorescent probe for reliable monitoring of gastrointestinal diseases in vivo, Biomater. 293 (2023), 121956.

[7] W.W. Liu, H.J. Xiang, M.X. Tan, Q.Q. Chen, Q.Q. Jiang, L. Yang, Y. Cao, Z.G. Wang, H.T. Ran, Y. Chen, Nanomedicine enables drug-potency activation with tumor sensitivity and hyperthermia Synergy in the second near-infrared biowindow, ACS Nano 15 (2021) 6457–6470.

[8] Y. Zheng, J. Chen, X.R. Song, M.Q. Chang, W. Feng, H. Huang, C.X. Jia, L. Ding, Y. Chen, R. Wu, Manganese-enriched photonic/catalytic nanomedicine augments synergistic anti-TNBC photothermal/nanocatalytic/immuno-therapy via activating cGAS-STING pathway, Biomater. 293 (2023), 121988.

[9] P.Y. He, Q. Lei, B. Yang, T.Y. Shang, J.J. Shi, Q. Ouyang, W. Wang, L.C. Xue, F. H. Kong, Z.Y. Li, J.D. Huang, L.H. Liu, J.M. Guo, C.J. Brinker, K.S. Liu, W. Zhu, Dual-stage irradiation of size-switchable albumin nanocluster for cascaded tumor enhanced penetration and photothermal therapy, ACS Nano 16 (2022) 13919–13932.

[10] T. Wu, T.Q. Lang, C. Zheng, W.L. Yan, Y. Li, R.Q. Zhu, X. Huang, H.E. Xu, Y.P. Li, Q. Yin, Promote intratumoral drug release and penetration to counteract docetaxel-induced metastasis by photosensitizer-modified red blood cell membrane-coated nanoparticle, Adv. Funct. Mater. 33 (2023), 2212109.

[11] J.C. Li, X.R. Yu, Y.Y. Jiang, S.S. He, Y. Zhang, Y. Luo, K.Y. Pu, Second near-infrared photothermal semiconducting polymer nanoadjuvant for enhanced cancer immunotherapy, Adv. Mater. 33 (2021), 2003458.

[12] C. Xu, Y.Y. Jiang, J.S. Huang, J.G. Huang, K.Y. Pu, Second near-infrared light-activatable polymeric nanoantagonist for photothermal immunometabolic cancer therapy, Adv. Mater. 33 (2021), 2101410.

[13] S.Y. Chen, Y.H. Pan, K. Chen, P.F. Chen, Q.M. Shen, P.F. Sun, W.B. Hu, Q.L. Fan, Increasing molecular planarity through donor/side-chain engineering for improved NIR-IIa fluorescence imaging and NIR-II photothermal therapy under 1064 nm, Angew. Chem. Int. Ed. 135 (2022), e202215372.

[14] P.F. Sun, F. Qu, C. Zhang, P.F. Cheng, X.Y. Li, Q.M. Shen, D.F. Li, Q.L. Fan, NIR-II excitation phototheranostic platform for synergistic photothermal therapy/chemotherapy/chemodynamic therapy of breast cancer bone metastases, Adv. Sci. 9 (2022), 2204718.

[15] S.J. Liu, H.L. Ou, Y.Y. Li, H.K. Zhang, J.K. Liu, X.F. Lu, R.T.K. Kwok, J.W.Y. Lam, D. Ding, B.Z. Tang, Planar and twisted molecular structure leads to the high brightness of semiconducting polymer nanoparticles for NIR-IIa fluorescence imaging, J. Am. Chem. Soc. 142 (2020) 15146–15156.

[16] J.G. Li, M.M. Kang, Z.J. Zhang, X. Li, W.L. Xu, D. Wang, X.K. Gao, B.Z. Tang, Synchronously manipulating absorption and extinction coefficient of semiconducting polymers via precise dual-acceptor engineering for NIR-II excited photothermal theranostics, Angew. Chem. Int. Ed. 62 (2023), e202301617.

[17] T.T. Sun, J.F. Han, S. Liu, X. Wang, Z.Y. Wang, Z.G. Xie, Tailor-made semiconducting polymers for second near-infrared photothermal therapy of orthotopic liver cancer, ACS Nano 13 (2019) 7345–7354.

[18] D. Cui, C. Xie, Y. Lyu, X. Zhen, K.Y. Pu, Near-infrared absorbing amphiphilic semiconducting polymers for photoacoustic imaging, J. Mater. Chem. B. 5 (2017) 4406–4409.

[19] M.H. Liu, Z. Zhang, Y.C. Yang, Y.H. Chan, Polymethine-based semiconducting polymer dots with narrow-band emission and absorption/emission maxima at NIR-II for bioimaging, Angew. Chem. Int. Ed. 60 (2021) 983–989.

[20] Y.N. Dai, H.H. Zhao, K. He, W.Y. Du, Y.J. Kong, Z. Wang, M.X. Li, Q.M. Shen, P. F. Sun, Q.L. Fan, NIR-II excitation phototheranostic nanomedicine for fluorescence/photoacoustic tumor imaging and targeted photothermal-photonic thermodynamic therapy, Small 17 (2021), 2102527.

[21] Y.Z. Xu, S.Y. Liu, L.L. Zeng, H.S. Ma, Y.F. Zhang, H.H. Yang, Y.C. Liu, S. Fang, J. Zhao, Y.S. Xu, C.R. Ashby, Y.L. He, Z. Dai, Y.H. Pan, An enzyme-engineered nonporous copper(I) coordination polymer nanoplatform for cuproptosis-based synergistic cancer therapy, Adv. Mater. 34 (2022) 2204733.

[22] J. Zhou, Q. Yu, J. Song, S. Li, X.L. Li, B.K. Kang, H.Y. Chen, J.J. Xu, Photothermally triggered copper payload release for cuproptosis-promoted cancer synergistic therapy, Angew. Chem. Int. Ed. 62 (2023), e202213922.

[23] S.P. Ning, M. Lyu, D.M. Zhu, J.W.Y. Lam, Q.Q. Huang, T.F. Zhang, B.Z. Tang, Type-I AIE photosensitizer loaded biomimetic system boosting cuproptosis to inhibit breast cancer metastasis and rechallenge, ACS Nano 17 (2023) 10206–10217.

[24] P. Tsvetkov, S. Coy, B. Petrova, M. Dreishpoon, A. Verma, M. Abdusamad, J. Rossen, L. Joesch-Cohen, R. Humeidi, R.D. Spangler, J.K. Eaton, E. Frenkel, M. Kocak, S.M. Corsello, S. Lutsenko, N. Kanarek, S. Santagata, T.R. Golub, Copper induces cell death by targeting lipoylated TCA cycle proteins, Science 375 (2022) 1254–1261.

[25] Q.X. Huang, J.L. Liang, Q.W. Chen, X.K. Jin, M.T. Niu, C.Y. Dong, X.Z. Zhang, Metal-organic framework nanoagent induces cuproptosis for effective immunotherapy of malignant glioblastoma, Nano Today 51 (2023), 101911.

[26] W.J. Xu, J.M. Qian, G.H. Hou, T.B. Wang, J.L. Wang, Y.P. Wang, L.J. Yang, X. K. Cui, A.L. Suo, A hollow amorphous bimetal organic framework for synergistic cuproptosis/ferroptosis/apoptosis anticancer therapy via disrupting intracellular redox homeostasis and copper/iron metabolisms, Adv. Funct. Mater. 32 (2022) 2205013.

[27] S. Sun, Q. Chen, Z.D. Tang, C. Liu, Z.J. Li, A.G. Wu, H.W. Lin, Tumor microenvironment stimuli-responsive fluorescence imaging and synergistic cancer therapy by carbon-dot-Cu2+ nanoassemblies, Angew. Chem. Int. Ed. 132 (2020) 21227–21234.

[28] B. Liu, Y.L. Bian, S. Liang, M. Yuan, S.M. Dong, F. He, S.L. Gai, P.P. Yang, Z. Y. Cheng, J. Lin, One-step integration of tumor microenvironment-responsive calcium and copper peroxides nanocomposite for enhanced chemodynamic/ion-interference therapy, ACS Nano 16 (2022) 617–630.

[29] Y. Xu, X.X. Han, Y.Y. Li, H. Min, X. Zhao, Y.L. Zhang, Y.Q. Qi, J. Shi, S. Qi, Y.P. Bao, G.J. Nie, Sulforaphane mediates glutathione depletion via polymeric nanoparticles to restore cisplatin chemosensitivity, ACS Nano 13 (2019) 13445–13455.

[30] W. Zhang, J. Lu, X.N. Gao, P. Li, W. Zhang, Y. Ma, H. Wang, B. Tang, Enhanced photodynamic therapy by reduced levels of intracellular glutathione obtained by employing a nano-MOF with Cu^{II} as the active center, Angew. Chem. Int. Ed. 57 (2018) 4891–4896.

[31] V. Oliveri, Biomedical applications of copper ionophores, Coord. Chem. Rev. 422 (2020), 213474.

[32] D.M. Zhu, R.Y. Ling, H. Chen, M. Lyu, H.S. Qian, K.L. Wu, G.X. Li, X.W. Wang, Biomimetic copper single-atom nanozyme system for self-enhanced nanocatalytic tumor therapy, Nano Res. 15 (2022) 7320–7328.

[33] F.F. Xia, A.X. He, H.T. Zhao, Y. Sun, Q. Duan, S.J. Abbas, J.J. Liu, Z.Y. Xiao, W. H. Tan, Molecular engineering of aptamer self-assemblies increases in vivo stability and targeted recognition, ACS Nano 16 (2022) 169–179.

[34] Y. Yang, B. Liu, Y. Liu, J.Q. Chen, Y.J. Sun, X.S. Pan, J. Xu, S.J. Xu, Z. Liu, W. H. Tan, DNA-based MXFs to enhance radiotherapy and stimulate robust antitumor immune responses, Nano Lett. 22 (2022) 2826–2834.

[35] C.Z. Liu, Y.X. Chen, J. Zhao, Y. Wang, Y.L. Shao, Z.N. Gu, L.L. Li, Y.L. Zhao, Self-assembly of copper-DNAzyme nanohybrids for dual-catalytic tumor therapy, Angew. Chem. Int. Ed. 60 (2021) 14324–14328.

[36] X. Men, F. Wang, H.B. Chen, Y.B. Liu, X.X. Men, Y. Yuan, Z. Zhang, D.Y. Gao, C. F. Wu, Z. Yuan, Ultrasmall semiconducting polymer dots with rapid clearance for second near-infrared photoacoustic imaging and photothermal cancer therapy, Adv. Funct. Mater. 30 (2020), 1909673.

[37] Y.E. Dai, F. Zhang, K. Chen, Z.Q. Sun, Z.H. Wang, Y.W. Xue, M.X. Li, Q.L. Fan, Q. M. Shen, Q. Zhao, An activatable phototheranostic nanoplatform for tumor specific NIR-II fluorescence imaging and synergistic NIR-II photothermal-chemodynamic therapy, Small 19 (2023), 2206053.